Materials Today Bio 8 (2020) 100082

Contents lists available at ScienceDirect

Materials Today Bio

journal homepage: www.journals.elsevier.com/materials-today-bio

Low dose novel PARP-PI3K inhibition via nanoformulation improves colorectal cancer immunoradiotherapy

M.R. Landry [a,f], A.N. DuRoss [a,f], M.J. Neufeld [a], L. Hahn [b], G. Sahay [a,c], R. Luxenhofer [b,d], C. Sun [a,e,*]

[a] Department of Pharmaceutical Sciences, College of Pharmacy, Oregon State University, Portland, 97201, OR, USA
[b] Department of Chemistry and Pharmacy, University Würzburg, Röntgenring 11, Würzburg, 97070, Germany
[c] Department of Biomedical Engineering, School of Medicine, Oregon Health & Science University, Portland, 97201, OR, USA
[d] Soft Matter Chemistry, Department of Chemistry, University of Helsinki, Helsinki, 00014, Finland
[e] Department of Radiation Medicine, School of Medicine, Oregon Health & Science University, Portland, 97239, OR, USA

ARTICLE INFO

Keywords:
Radiation therapy
Immune checkpoint blockade
Poly(2-oxazoline)
Nanomedicine
Drug delivery

ABSTRACT

Multimodal therapy is often used in oncology to overcome dosing limitations and chemoresistance. Recently, combination immunoradiotherapy has shown great promise in a select subset of patients with colorectal cancer (CRC). Furthermore, molecularly targeted agents delivered in tandem with immunotherapy regimens have been suggested to improve treatment outcomes and expand the population of responding patients. In this study, radiation-sensitizing small molecules niraparib (PARP inhibitor) and HS-173 (PI3K inhibitor) are identified as a novel combination that synergistically enhance toxicity and induce immunogenic cell death both *in vitro* and *in vivo* in a CRC model. These inhibitors were co-encapsulated in a polymer micelle to overcome solubility limitations while minimizing off-target toxicity. Mice bearing syngeneic colorectal tumors (CT26) were administered these therapeutic micelles in combination with X-ray irradiation and anti-CTLA-4 immunotherapy. This combination led to enhanced efficacy demonstrated by improved tumor control and increased tumor infiltrating lymphocytes. This report represents the first investigation of DNA damage repair inhibition combined with radiation to potentiate anti-CTLA-4 immunotherapy in a CRC model.

1. Introduction

The aggressive proliferation and spread of late-stage cancers are seldom controlled by one therapeutic modality alone. Current clinical oncology practice typically employs two or more therapies sequentially or concurrently, which necessitates a balance of treatment safety and efficacy. Patients diagnosed with advanced disease often undergo a combination of radiation, chemo-, immuno-, and molecularly targeted therapies. In the case of colorectal cancer (CRC), late-stage presentation occurs in 60% of patients when curative surgical resection is not feasible, thus requiring multimodality treatment [1]. The advanced age of patients with CRC (average 65–74 yrs) at diagnosis further complicates treatment and highlights the need for safer therapeutic regimens [1].

Immunotherapy has begun to address the need in CRC treatment for effective tumor killing with increased durability. Specifically, immune checkpoint blockade (ICB) recently demonstrated improved survival for a subset of patients with CRC compared with traditional chemo- and radiation therapy (RT) [2–5]. As a result, the combination of ipilimumab (anti-CTLA-4) and nivolumab (anti-PD-1) was approved for microsatellite instability (MSI)-high or mismatch repair (MMR)-deficient metastatic CRC in 2018 [6]. Although promising, two major limitations persist for this ICB-based therapy. First, the approved combination resulted in immune-related adverse effects (irAEs) in the majority of patients. In this case and others, CTLA-4 antibodies are dose limited due to the high occurrence of grade 3 and 4 irAEs [3,7]. Second, positive outcomes are limited to the small subset of patients (MSI-high and MMR-deficient) who have high mutational burden and increased metastases [6].

The integration of DNA damaging agents, such as ionizing radiation (IR) and chemotherapy, into immunotherapy regimens to potentiate immunogenic cell death (ICD) and subsequently synergistically enhance therapy has been of significant interest recently [8]. In the context of CRC, the addition of poly-ADP ribose polymerase (PARP)

* Corresponding author. Department of Pharmaceutical Sciences, College of Pharmacy, Oregon State University, Portland, 97201, OR, USA.
E-mail address: sunc@ohsu.edu (C. Sun).
[f] Madeleine R. Landry and Allison N. DuRoss have contributed equally to this work.

https://doi.org/10.1016/j.mtbio.2020.100082
Received 27 July 2020; Received in revised form 20 September 2020; Accepted 8 October 2020
Available online 22 October 2020

inhibitors to these genotoxic treatments is actively being investigated [9]. Taken together, this presents an opportunity to combine immunotherapy and RT with PARP inhibition for enhanced patient responses and outcomes. On a molecular level, PARP is responsible for repairing single strand breaks (SSBs) resulting from defects in the DNA damage response (DDR) pathway or induced by exogenous agents, such as IR. In addition to preventing the repair of DNA damage, PARP inhibitors play an activating role in the immunostimulatory cyclic GMP-AMP synthase–stimulator of interferon genes pathway [10]. Inhibition of PARP in irradiated cells has been shown to enhance efficacy by both increasing type 1 interferon production and radiation-induced SSB accumulation [11]. Ultimately, these processes lead to cell death and the potential to convert so-called 'cold' non-immunogenic tumors to 'hot' immunogenic tumors.

As a monotherapy, the utility of PARP inhibitors is limited to patients with defective homologous recombination DNA repair. To broaden their application, phosphoinositide-3-kinase (PI3K) inhibitors have been shown to sensitize tumors with proficient DDR to PARP inhibition [12–14]. Furthermore, in combination with RT, we and others have previously demonstrated the radiosensitizing potential of combining PI3K and PARP inhibitors [15–17]. Here, for the first time in a CRC model, we performed a combinatorial analysis of several PARP and PI3K inhibitors to determine the optimally synergistic and radiosensitizing pair. Upon screening in an MMR proficient CRC cell line both with and without RT, niraparib (N), a PARP inhibitor FDA approved for ovarian cancer, and HS-173 (H), an experimental drug developed as an imidazopyridine-based PI3Kα inhibitor, were identified as a potent combination, hereinafter referred to as N-H [18].

Unfortunately, similar to many other small molecule inhibitors, N and H are extremely hydrophobic, necessitating the use of potentially cytotoxic (co-)solvents and excipients. These formulation vehicles, such as Cremophor EL, have limited solubilization capabilities and narrow the already restricted therapeutic window [19]. Polymeric micelles are an ideal alternative drug carrier; Genexol-PM is one such example where polymeric micelles outperformed Cremophor EL in terms of patient response and toxicity when delivering paclitaxel [19]. Here we use poly(2-oxazoline) (POx) based amphiphiles to encapsulate N-H in a micelle-based formulation to improve solubility and facilitate *in vivo* drug delivery. POx polymers are a promising class of solubilizing agents with physiochemical properties optimized for pharmaceutical formulations [20,21]. Recently, the utility of POx polymers has grown due to their facile synthesis and tunability. In particular, ABA-type triblock copolymers bearing a hydrophilic shell (poly(2-methyl-2-oxazoline)) and differing hydrophobic cores enable high encapsulation efficiency in a micellar formulation for various drugs [22]. In addition to improved pharmacokinetics and biodistribution, the novel N-H POx formulation maintains favorable stability and cellular uptake characteristics, while addressing the main aim of increasing on-target drug concentrations with limited off-target toxicities.

In this study, we investigated the utility of N-H POx to enable a multipronged CRC treatment strategy. In addition to prerequisite physical and chemical characterization, a preclinical evaluation was performed in a syngeneic mouse model to assess both tumor cell killing of adding N-H POx and IR to CTLA-4 therapy (α-CTLA-4), and the treatment's overall safety. Codelivery of PARP and PI3K inhibitors may both selectively induce an MMR-deficient state in an MMR-proficient cell line and induce ICD. Therefore, exploiting PARP/PI3K inhibition has the potential to expand the responding population to include microsatellite stable patients with CRC. Herein, we demonstrate that this novel PARP/PI3K inhibitor combination delivered via POx micelles provides an added benefit to anti-CTLA-4 immunotherapy in a syngeneic murine CRC model.

2. Experimental

2.1. Materials

The POx polymer, A-PBzOx-A, was synthesized as previously described [45]. Crystal violet dye, acetonitrile high-performance liquid chromatography (HPLC grade), TFA, and methanol (HPLC grade) were purchased from Fisher Scientific (Hampton, NH, USA). Cyanine 7.5 carboxylic acid was purchased from Lumiprobe (Hunt Valley, MD, USA), niraparib was purchased from MedChemExpress (Monmouth Junction, NJ, USA) and HS-173 was purchased from MedChemExpress and Selleck Chem (Houston, TX, USA). Anti-CTLA-4 antibody (9D9 clone) was purchased from Bio X Cell (West Lebanon, NH). Phosphate-buffered saline (PBS) 1X and RPMI 1640 medium were purchased from Corning Inc. (Corning, NY, USA). Amicon Ultra centrifugal filters and 10% (v/v) neutral buffered formalin were obtained from Millipore Sigma (Burlington, MA, USA). DAPI (4′,6-Diamidino-2-Phenylindole, Dilactate) and Alexa Fluor™ 488 Phalloidin were purchased from Thermo Fisher Scientific (Carlsbad, CA, USA). CT26 cells were purchased from ATCC and maintained in RPMI 1640 medium supplemented with 10% (v/v) fetal bovine serum and 1% (v/v) penicillin/streptomycin.

2.2. In Vitro cytotoxicity

To determine the efficacy of PARP and PI3K combinations, CT26 cells were seeded at 2000 cells per well in two replicate 96-well plates per combination and allowed to settle overnight. Cells were then treated with free drugs (alone or in combination) at various concentrations ranging from 0.01 μM to 50 μM (Fig. 1B and S1) and incubated at 37 °C. After 24 h, a radiation dose of 4 Gy was administered to one of the replicate plates. After 48 h, cells were washed once with PBS, then viability was determined by Alamar Blue (Invitrogen, Eugene, OR, USA). Sample fluorescence at 530 and 590 nm was measured using an Infinite M200 Pro plate reader (Tecan US Inc, Morrisville, NC, USA). Cell viability was normalized to untreated cells, and IC50 values were computed by fitting the data to a four-parameter dose response, variable slope model using GraphPad Prism 8. Combination indexes (CIs) were determined using CompuSyn (ComboSyn Inc, Paramus, NJ, USA), where cell viabilities less than 90% and greater than 10% were the only Fa values used. All cell viability measurements were performed in triplicate.

Free N-H, E POx, and N-H POx viability were run the same as described previously. Concentrations of N-H (solubilized in dimethyl sulfoxide (DMSO) or encapsulated in micelle) ranged from 0.0003 μM to 100 μM. E POx dosing matched that of the N-H POx in terms of polymer concentration.

2.3. In Vitro ICD assay

CT26 cells were plated in at 25,000 cells/well in an 8-well chamber slide and allowed to settle for 24 h. At 24 h, media was replaced with media containing N-H (0.4 μM each), oxaliplatin (50 μM) as a positive control, or media as a negative control. Cells were incubated for 6 h, and then cells were washed with PBS twice and formalin fixed. Cells were incubated with Hoechst (33,342, Invitrogen) diluted in RPMI at 5 μg/mL for 10 min, followed by incubation with wheat germ albumin (WGA) (W11261, Invitrogen) diluted in Hank's Balanced Salt Solution at 5 μg/mL to stain the nuclei and cell membrane, respectively. Cells were then incubated with a rabbit anti-Calreticulin antibody (ab2907, Abcam) at a 1:200 dilution for 30 min on ice in non-permeabilizing antibody dilution buffer (1% BSA in PBS). Then, cells were washed with PBS and incubated with a goat anti-rabbit IgG H&L (Cy 5) antibody (6564, Abcam) at a 1:1000 dilution in non-permeabilizing antibody dilution buffer in the dark for 30 min at room temperature. Finally, cells were once more washed with PBS and imaged using an EVOS FL Auto microscope at 40× magnification.

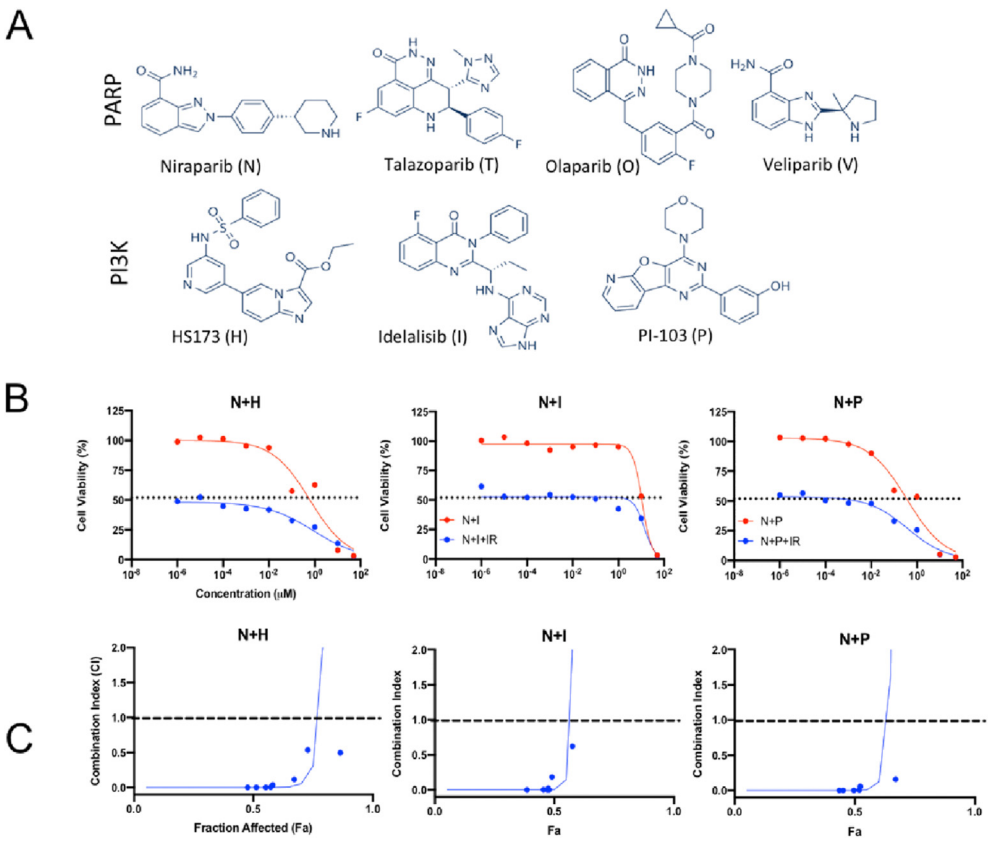

Fig. 1. Evaluation of cell viability and drug synergy. (**A**) Chemical structures of PARP and PI3K inhibitors **(B)** *In vitro* toxicity of free drug combination treatment with (●) and without (●) radiation. Radiation only controls are shown with a dotted line. **(C)** Combination index (CI) values with radiation were calculated and plotted to evaluate the synergy of the combination with radiation. CI > 1 represents antagonism, CI = 1 represents additivity, and CI > 1 represents synergy. The dashed line is for reference at y = 1. The full screen combination data are in Fig. S1. The N and H combination was chosen due to data in both (B) and (C).

2.4. Preparation and characterization of drug encapsulated micelles

Polymeric micelles were prepared via a modified nanoprecipitation method. To formulate N-H POx, A-PBzOx-A polymer was solubilized in ethanol at 300 mg/mL, while niraparib and HS-173 were solubilized individually in DMSO at 30 mg/mL. An organic layer was prepared by first combining N and H, then adding the polymer and excess ethanol, followed by sonication. To achieve micelle formation, PBS was added to the organic layer at a 9:1 PBS:organic v/v ratio for a polymer concentration of 5 mg/mL and drug concentrations of 1 mg/mL each. The micelles were subsequently filtered at 4696 × G for 10 min and 22 °C using a 10,000 kDa MW cutoff Amicon Ultra centrifugal filter to remove solvent and free drug/polymer. Following centrifugation, the micelles were resuspended to the precentrifugation volume in PBS. Empty micelles (E POx) were prepared in the same manner with equal DMSO in the place of N and H. Cy7.5 POx (Cy7.5 loaded micelles) were also prepared as described previously, substituting drug for a stock of Cy7.5 in DMSO at 1 mg/mL. The final concentration of the Cy7.5 in the micelles was 0.01 mg/mL.

Purified micelles were characterized by DLS, transmission electron microscopy (TEM). DLS was performed using a Malvern Nano ZSP (Malvern Panalytical, Malvern, UK) to determine the size, zeta potential, and polydispersity for micelle formulations. TEM images were obtained with a Tecnai iCorr while cryoTEM images were obtained with a Titan Krios Cryo-TEM (FEI, Hillsboro, OR, USA). Drug loading was quantified using a Shimadzu SPD-20A HPLC instrument (Torrance, CA, USA) equipped with a UV/Vis detector and an Agilent Zorbax Rapid Resolution SBC-18 column (4.6 × 100 mm 3.5 μm; Santa Clara, CA, USA). The filtrate from centrifugally filtered micelles was diluted in a 100-fold in MeOH and analyzed by HPLC. To ensure the drug was properly quantified, the filter was flooded with 2 mL MeOH twice and run on HPLC to ensure all drug was accounted for. All samples were compared with a standard curve of N and H to determine concentration. The samples were run with a 65%–70% methanol in water (0.1% TFA) gradient over 6 min with a flow rate of 1 mL/min and a 311 nm detection wavelength. Niraparib eluted first (retention time = 1.3 min) with HS-173 following (retention time = 2.3 min).

2.5. In vitro drug release

Drug release for the two inhibitors was determined by loading micelles into Slide-A-Lyzer MINI dialysis microtubes with a molecular weight cutoff of 2 kDa. N-H POx samples were dialyzed against a 120-fold excess of buffer (pH 5.5, 6.8, or 7.4 PBS) with gentle stirring in a water bath at 37 °C. Samples of 1 mL were collected at designated time points between 0 and 360 h, diluted in methanol (1:4), and concentrations determined by HPLC as previously described previously. Drug release profiles were plotted as a cumulative percentage of total drug release versus time. All drug release measurements were performed in triplicate.

2.6. In vitro cellular uptake study

CT26 cells were seeded into a 96-well plate (6000 cells/well) and allowed to settle for 24 h. When cells had settled, Cy-7.5 POx and free Cy7.5 (both at a constant 1000 ng/mL concentration) were added in fresh media at various time points between 0 and 24 h. At study end point, the cells were washed with PBS, formalin fixed, and imaged on EVOS FL Auto microscope at 20× magnification. Images were processed using ImageJ, and the average pixel intensity of 6 images (2 per well) for each time point were calculated and graphed.

2.7. Clonogenic assay

The radiosensitizing ability of N-H POx was assayed by seeding CT26 cells into T25 flasks, which were allowed to settle overnight and subsequently treated for 24 h. After therapeutic incubation, cells were

trypsinized, seeded into 6-well plates, and irradiated (CellRad X-ray Cabinet Irradiator, Faxitron, 130 kV, 5 mA, 0.5 mm aluminum filter, ~1.2 Gy/min). The irradiated cells were then allowed to proliferate for 7 days. The number of cells seeded varied based on the dose of radiation (0–8 Gy) and drug treatment condition (media only, 0.4 μM free niraparib, 0.4 μM free HS-173, 0.3/0.4 μM free niraparib/HS-173, 0.3/0.4 μM N-H POx, and 1.8 mg/mL E POx further diluted to the same concentration as N-H POx were dosed at). The plating numbers ranged from 100 cells/well for no treatment to 3000 cells/well for 8 Gy plus N-H POx. At study end, cells were washed with PBS, formalin fixed, and stained with 0.01 mg/mL crystal violet dye to identify colonies of greater than 50 cells. The survival fraction (SF) was determined by calculating an average plating efficiency (PE) for each treatment and dividing that value by the average PE of the unirradiated control for each drug treatment. Here, PE is the number of colonies formed for a condition divided by the number of cells seeded for that condition.

2.8. Immunofluorescent γH2AX DNA damage assay

To evaluate DNA double-strand breaks (DSBs), CT26 cells were plated at 120,000 cells/well in two gelatin-coated 4-well chamber slides and allowed to settle for 24 h. At 24 h, media was replaced with media containing N-H, N-H POx, E POx, or media only. Cells were incubated with these treatments (Fig. 4) for 20 h at which point one of the plates was irradiated with 2 Gy (CellRad). Fifteen minutes after irradiation, cells were washed with PBS and formalin fixed. After fixing, cells were again washed with PBS, then blocked and permeabilized using 5% goat serum and 0.3% Triton X-100. After blocking and permeabilization, cells were incubated with a rabbit anti-Phospho-Histone H2AX (Ser139) Antibody (#2577, Cell Signaling Technologies) at a 1:800 dilution for 2 h at room temperature in antibody dilution buffer (1% BSA and 0.3% Triton X-100 in PBS). Then, cells were washed with PBS and incubated with a goat antirabbit IgG H&L (Cy 5) antibody (6564, Abcam) at a 1:1000 dilution in antibody dilution buffer in the dark overnight at 4C. Finally, the cells were stained with DAPI and Phalloidin, washed once more with PBS, and imaged using an EVOS FL Auto microscope at 20× magnification. DNA quantification was assessed using CellProfiler overlaying DAPI stained nuclei with Cy5-stained γH2AX foci for a foci/cell count using a modified speckles pipeline.

To analyze γH2AX by flow cytometry, 500,000 cells were plated in 6-well plates. After 24 h, cells were dosed with N-H, N-H POx, E POx, or media in triplicate. After 20 h of incubation, half of the plates were irradiated with 2 Gy. Fifteen minutes later, cells were detached from the plate using trypsin/EDTA and diluted in media. The cells were pelleted at 500×*g* for 5 min, the media was aspirated, and the cells dispersed in PBS. This process was repeated this time substituting formalin for PBS to allow fixation for 15 min. To remove fixative, cells were again pelleted at 500×*g* for 5 min, the formalin aspirated and cells dispersed in antibody dilution buffer containing the above γH2AX primary antibody at 1:800 dilution. After 2 h at room temperature, the antibody was removed by pelleting, then the cells were washed and redispersed in a PBS solution of DAPI. Ten minutes later, the cells received one final spin at 500×*g* for 5 min, the DAPI was aspirated, the cells were resuspended in PBS and strained through a filter cap into 8 mL flow cytometry tubes. Samples were assessed using a MACSQuant flow cytometer (Miltenyi Biotec, Cologne, Germany). Fluorescence of no treatment, E POx, N-H, N-H POx, and/or irradiated cells was determined using a 632 nm excitation laser line, with a 655–730 nm emission filter set. Forward scattering/side scattering were used to identify live, single cells passing through the detector, and 100,000 cells were evaluated in the flow cytometer for each sample to build a distribution.

2.9. In vivo studies

All animal studies were approved by and conducted in accordance with the guidelines of the Institutional Animal Care and Use Committee (IACUC) of Oregon Health and Sciences University. For all imaging studies and when noted, mice were anesthetized using 2–3% isoflurane (Piramal Enterprises Limited, Telangana, India).

2.10. Establishment of tumor xenografts in mice

Subcutaneous CT26 tumor xenografts were established by injecting cell suspensions (150,000 cells) into the right flanks of BALB/c mice (Charles River Laboratories, Wilmington, MA).

2.11. In vivo ICD

One female BALB/c mouse was implanted with 150,000 CT26 cells on the right hind flank. 12 days after implant, the mouse had developed two sizable tumors. One of the tumors was injected with N-H suspended in

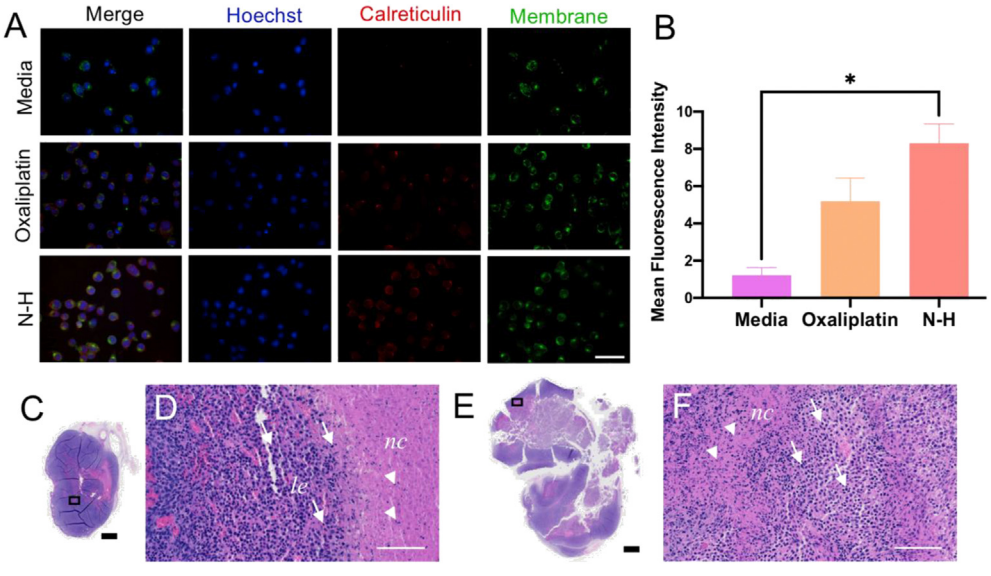

Fig. 2. Immunogenic cell death induction *in vitro* and *in vivo*. **(A)** Visualization of immunogenic cell death by surface (wheat germ albumin membrane stain) exposure of calreticulin. **(B)** Quantified calreticulin expression for each treatment group from images in (A). * denotes significance ($p < 0.05$) **(C)** Macroscopic view of DMSO-treated tumor demonstrates dense tumor tissue (purple) with a small necrotic region (pink). **(D)** Microscopic view of rectangle in (C) which demonstrates the accumulation of leukocytes (purple specks) at the necrotic region (pink) periphery with minimal infiltration. **(E)** Macroscopic view of N-H treated tumor demonstrates less dense tumor tissue (purple) and a larger necrotic region (pink). **(F)** Microscopic view of (E) demonstrates a larger leukocyte (purple specks) influx to the necrotic region (pink). *le* represents the leading edge of immune infiltration, and *nc* represents the necrotic region. Arrows represent leukocytes and arrowheads represent nuclear fragments. Scale bars represent 1000 μm (black) and 100 μm (white).

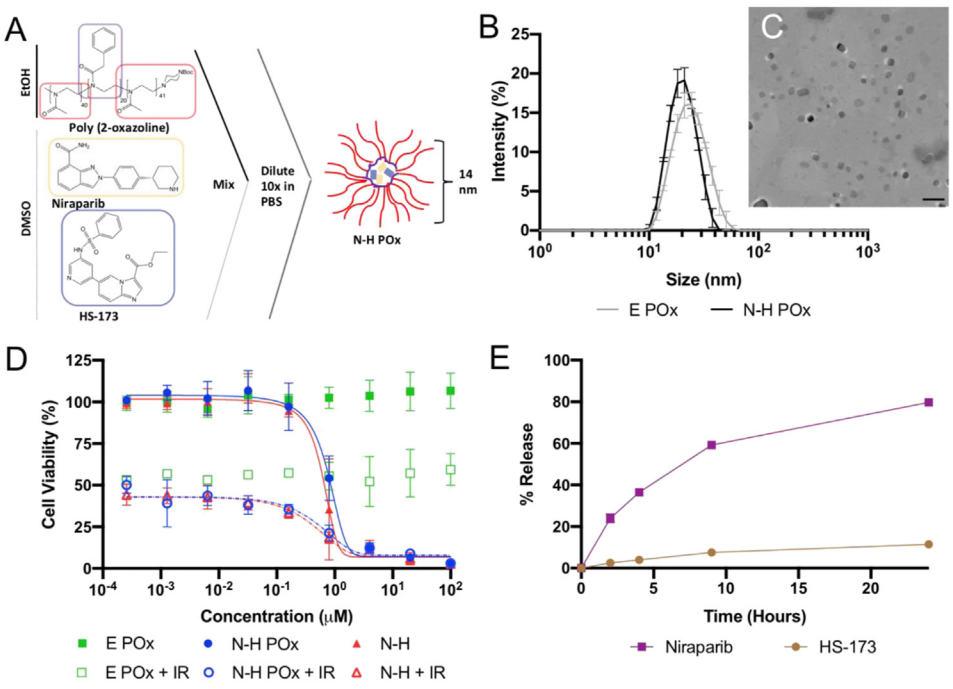

Fig. 3. Particle characterization. (**A**) Schematic representation of formulation method showing structure of drugs, polymers, and micelles. **(B)** Intensity average DLS measurements for E and N-H POx. **(C)** Negative stain TEM image of N-H POx demonstrates a particle size of about 14 nm. Scale bar represents 100 nm. **(D)** *In vitro* toxicity of free N-H compared with E and N-H POx, with (open symbols) and without radiation (closed symbols). **(E)** Drug release profile for N-H POx under sink conditions at pH 7.4 PBS as determined by HPLC.

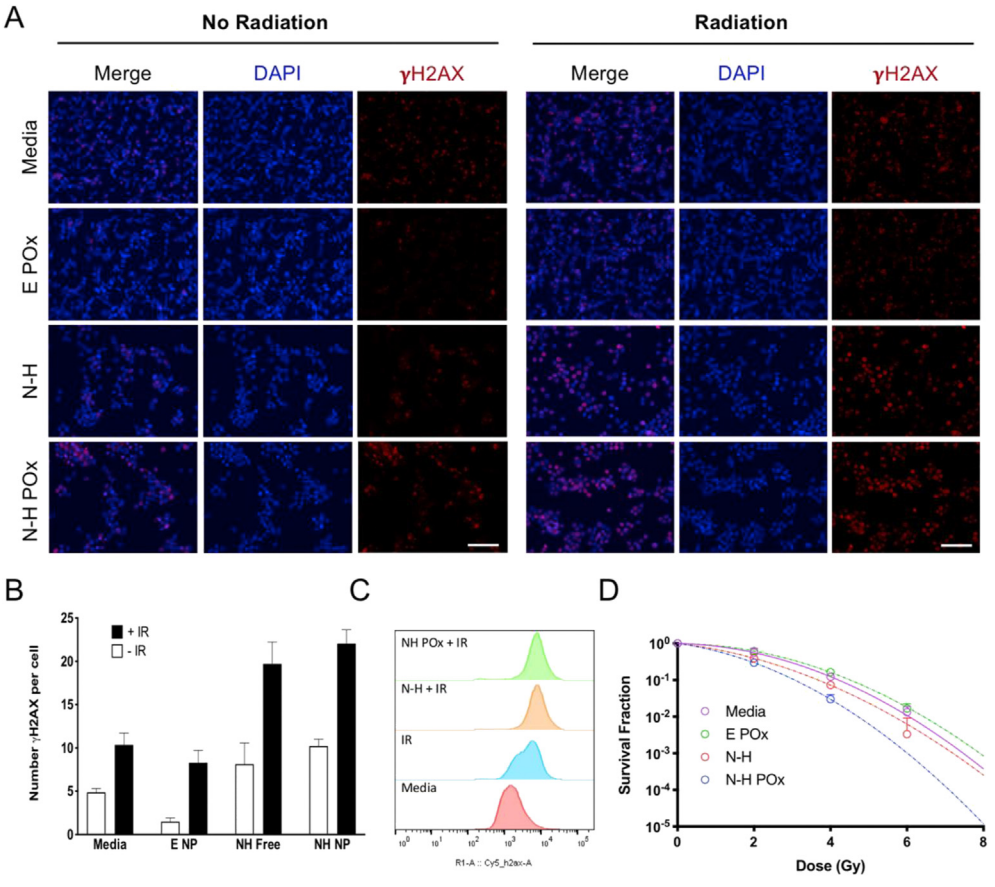

Fig. 4. ***In vitro*** **radiation and N-H combination damage.** (**A**) Representative γH2AX images demonstrate the difference in number of foci and overall signal intensity for various treatments with and without radiation. Scale bar represents 100 μm. **(B)** Quantification of γH2AX puncti per cell from images in (A). **(C)** Histograms of treated samples analyzed by flow cytometry show shift in γH2AX intensity. **(D)** Clonogenic assay demonstrates the radiosensitizing potential of N-H POx over free N-H or E POx at various radiation doses. Curves are fit using the linear quadratic equation. No colonies formed in the N-H POx treatment group at 6 gray.

PBS and DMSO and the other with an equal amount of DMSO. N-H was administered at a dose estimated to be deliverable using the N-H POx formulation by IV, assuming that a maximum of 10% would reach the tumor. Tumors were harvested 24 h later and formalin fixed at 4 °C overnight before being transferred to 70% ethanol. At this point, tissues were submitted to the OHSU Histopathology Shared Resource Core for tissue clearing, slicing (5 μm), and subsequent hematoxylin and eosin (H&E) staining. Imaging was performed on a Zeiss Axio Scan.Z1 Slide Scanner by the OHSU Advanced Light Microscopy Core at 20 ×.

2.12. Evaluation of safety in mice

Toxicity of the various treatment regimens were evaluated in six-week-old, female, tumor-bearing BALB/c mice aged 6-weeks. Mice were treated with E POx or N-H POx and each of the following conditions: alone, with radiation only, with CTLA-4 only, or with both radiation and CTLA-4 as detailed in Fig. 5A. Fourteen days after the start of treatment, mice were anesthetized, and blood was collected into 1 mL lithium heparin coated tubes (Grenier Bio-One, Kremsmünster, Austria) via cardiac puncture and stored at 4 °C before hematology and complete blood counts (CBC) analysis by IDEXX Laboratories.

2.13. Evaluation of antitumor efficacy and long-term effects in mice

For the first *in vivo* study (Fig. 5), 76 six-week old BALB/c mice were injected subcutaneously with 150,000 CT26 cells on the right hind flank. Seven days after CT26 tumor inoculation, 41 mice were randomized to receive α-CTLA-4 treatment and injected intraperitoneally with 250 μg anti-CTLA-4 antibodies. Five days later, all 76 mice were randomized into one of eight treatment groups ($n \geq 7$ per group, Fig. S9B). These eight treatment groups were further randomized into a treatment efficacy/safety study (32 mice, $n = 4$ per group) and survival (44 mice, $n \geq 3$ per group) study. On the day that the first mouse from the 32 mice randomized to treatment efficacy/safety reached an endpoint all 32 mice were sacrificed, with organs and blood harvested to evaluated safety and efficacy. On day 14, two mice reached an endpoint, so all 32 mice were sacrificed with the two who reached endpoints being included in the survival study (bringing the total to 46 mice) but all 30 other mice being excluded as they would have survived longer. As the 44 mice in the survival study and the 32 all survived to day 14, these mice were all included in the tumor growth curves.

For tumor volume/efficacy/survival studies, treatment groups were as follows: (1) E POx control, (2) E POx + IR, (3) niraparib and HS-173 micelles (N-H POx), (4) N-H POx + IR, (5) E POx + α-CTLA-4, (6) E POx + IR + α-CTLA-4, (7) N-H POx + α-CTLA-4, or (8) N-H POx + IR + α-CTLA-4. Mice were administered micelles via tail vein injection 3 × on days 0, 2, and 4 for a total of 10.73 mg/kg HS-173 and 11.07 mg/kg niraparib. Mice in groups 2, 4, 6, and 8 were irradiated with 1 Gy on days 0, 2, and 4 for a total of 3 Gy. Radiation was delivered (CellRad, Faxitron, 130 kV, 5 mA, 0.5 mm aluminum filter, ~1.2 Gy/min) selectively to tumors by covering mice with half-moon cutout lead shields (Precision X-Ray, North Branford, CT). Mouse body

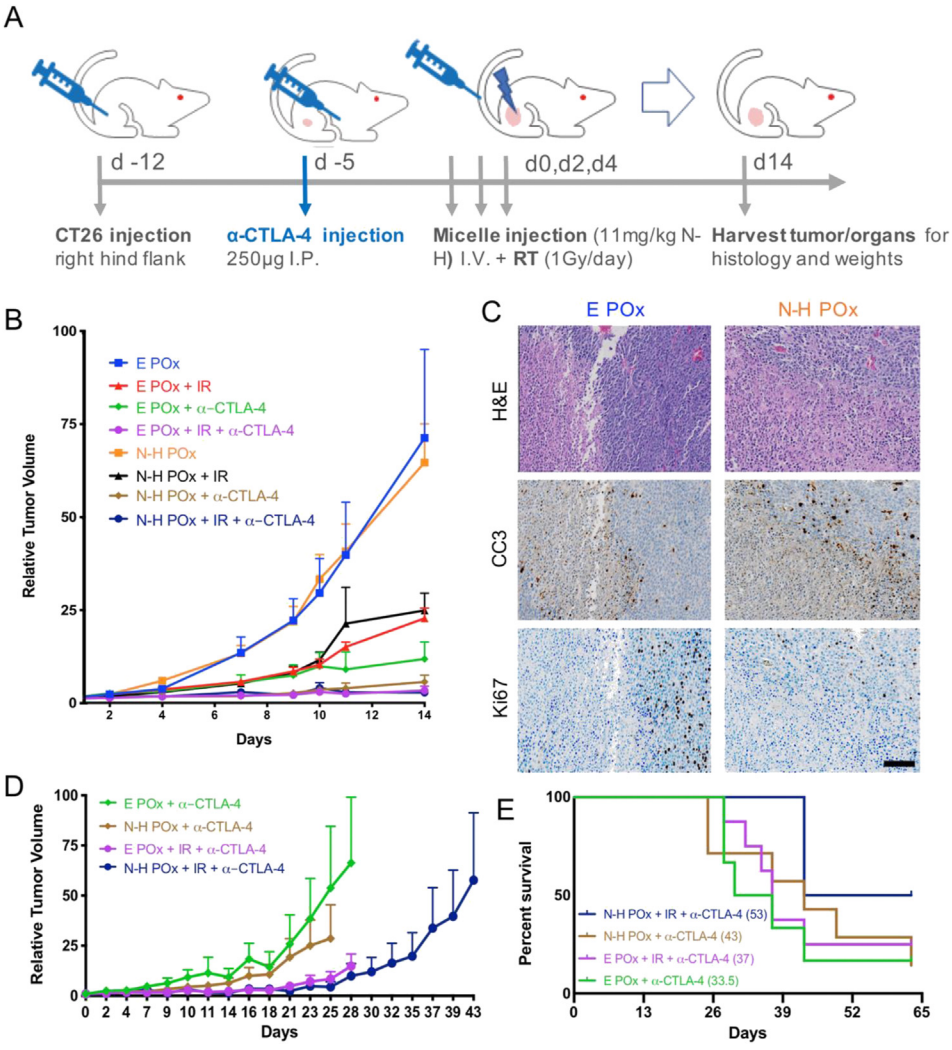

Fig. 5. *In vivo* efficacy and survival studies. **(A)** Dosing schedule for both the efficacy and survival studies. **(B)** Relative tumor volume curves for mice in efficacy study treated with various therapeutic agents after treatment regimen in (A). **(C)** Polymer carrier (E POx) and N-H POx–treated tumors from day 14 stained with H&E, proliferation (Ki67 in brown), and apoptosis (CC3 in brown). Scale bar (100 μm) is representative for all images. **(D)** Relative tumor volume for α-CTLA-4 treatment groups from survival study. Curve ends when first mouse in treatment group reaches the endpoint. **(E)** Kaplan-Meier survival curve for α-CTLA-4 treatment groups with differences in survival calculated in accordance with the logrank test.

weight and average tumor diameter (1/2 × length × width^2) were recorded 2–3 times per week. As mentioned previously, tumor measurements from both the survival and efficacy groups were used to generate relative tumor growth curves up to day 14. On day 14, the first mouse reached an endpoint, and the efficacy mice were sacrificed. Terminating the efficacy study when the first mouse reached an endpoint allowed for a direct comparison of tumor growth inhibition based on tumor volume curves, as well as endpoint tumor mass and histologic parameters. Mice were euthanized per IACUC guidelines once tumors began to develop cavitated ulcerations, weight loss reached 20% of starting weight, or any diameter reached 2 cm. Cardiac puncture was used to collect terminal blood samples for clinical chemistry. Organs from at least one mouse per treatment group were harvested for H&E staining to evaluate therapeutic toxicity and hypoxia. In addition, tumors from these mice were stained for Ki67 and Cleaved Caspase-3 to evaluate proliferation or apoptosis, respectively (see Tumor Histology below). A Kaplan-Meier curve was developed for each treatment group to examine differences in survival.

For the second *in vivo* study, 28 mice were implanted with CT26 tumors as described previously. Half of the mice were injected with CTLA-4 antibodies 7 days after tumor implant (mimicking study 1) and the other half 12 days after tumor implant, concurrent with the start of radiation and micelles. The mice followed the same radiation and micelle dosing as aforementioned, with caliper measurements of the tumors 2–3 times weekly. The mice tumor growth curves (Fig. 6B) were carried out until one of the mice reached an endpoint in one particular group, rather than all groups. Individual growth curves were carried out until all of the mice reached an endpoint or were cured. At day 58, cured mice were challenged with 150,000 CT26 cells on the right hind flank, similarly to initial tumor inoculation. The mice were monitored for 30 days for regrowth of a tumor.

2.14. Tumor histology

Tumors from mice in the tumor volume treatment protocol were collected and formalin fixed at 4 °C overnight before being transferred to 70% ethanol and submitted to the OHSU Histopathology Shared Resource Core for tissue clearing, slicing (5 μm), and subsequent staining. Stains performed were hematoxylin and eosin (H&E), Caspase-3 (Promega), and Ki67 (Cell Marque). Antibodies were diluted in accordance with supplier recommendations before staining. Imaging was performed on a Zeiss Axio Scan.Z1 Slide Scanner by the OHSU Advanced Light Microscopy Core at 20 ×.

2.15. Statistical analysis

All data are expressed as mean ± SEM. Statistical differences and significance were evaluated using one-way ANOVA, two-way ANOVA, or *t*-test in the Graph Pad Prism 8 software pack. $p < 0.05$ was considered statistically significant and represented by *.

3. Results and discussion

3.1. PARP and PI3K inhibitor combination screen and cell viability

Currently, only antiangiogenic therapeutics are approved and used as molecular therapies for CRC. As mentioned previously, PARP is under investigation as a target for CRC treatment, while PI3K is often upregulated in CRC making the combination of inhibitors targeting these proteins a promising therapeutic strategy [23–26]. To optimize this potential therapy, a combinatorial array of four PARP and three PI3K inhibitors were evaluated for synergy in murine CT26 cells (Fig. S1A). Here the cytotoxic effects of the drug combinations both with and without concomitant IR of 4 gray (Gy) were assessed to determine radiosensitization (Fig. S1B). All of the PARP-PI3K combinations yielded an increase in cell death with the addition of radiation. Of the PARP inhibitors tested, N combinations in particular resulted in greatly enhanced toxicity with radiation. In contrast, olaparib, and veliparib combinations resulted in minimal enhancement of radiation induced cell killing and were eliminated from consideration.

Next, CI values were derived and evaluated to further narrow potential combinations. The CI values were calculated by comparing the response of cells to individual drugs versus combinations at specific concentrations (Fig. S1C). These pairings can be synergistic (CI < 1), additive (CI = 1), or antagonistic (CI > 1). If the cellular response is stronger at a combination concentration than the sum of responses to each drug alone at the same concentration, it is considered synergistic. Although talazoparib combinations were especially toxic, they were largely not synergistic upon the addition of radiation (the graph curves back up), similar to N with PI-103. With two viable combinations remaining, the N-H (PARP-PI3K inhibitor) combination was selected

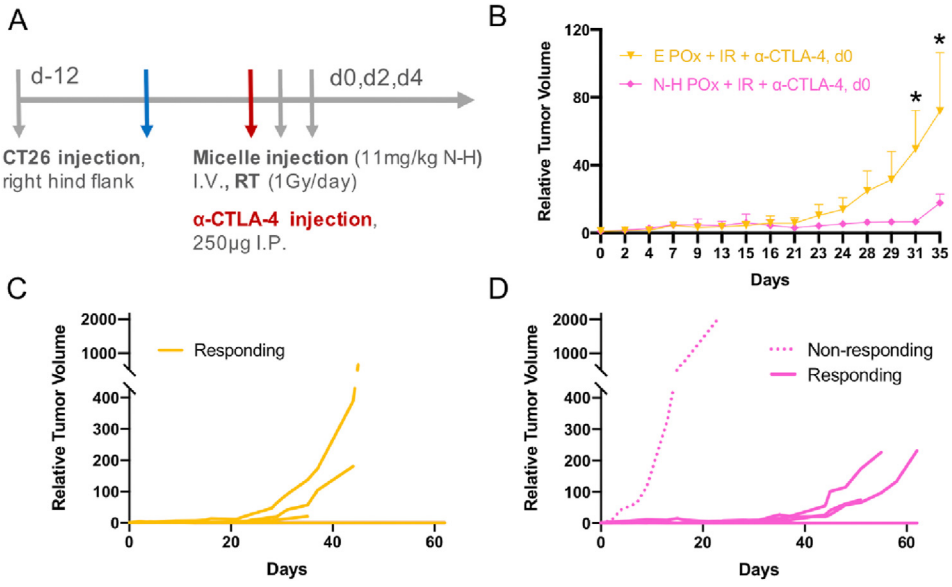

Fig. 6. Alternative α-CTLA-4 dosing study. (A) Treatment scheme similar to Fig. 5A with altered α-CTLA-4 dosing time. **(B)** Relative tumor volume curves for uncured mice responding to treatment (n = 3), * denotes $p < 0.016$. **(C)** Individual growth curves for all (cured and uncured) E POx + IR + α-CTLA-4 treated mice. **(D)** Individual growth curves for all (cured and uncured) N-H POx + IR + α-CTLA-4–treated mice. The dotted curve represents a non-responding mouse. Responding, uncured mice in (D) show delayed growth versus responding, uncured mice in (C).

based on consideration of CI, cell viability, and H-specific properties. At low concentrations, the N-H combination (Fig. 1A) elicited minimal response but upon irradiation saw a sharp decrease in cellular viability (Fig. 1B). Across a broad range of concentrations tested, N and H at a 1:1 ratio produced CI values less than one, indicating synergy (Fig. 1C). The synergistic effects were especially prominent at higher fractions affected, which is more relevant for anticancer agents [27]. Clinically, this response profile would capitalize on the conformal nature of RT to induce maximal response at the focal points of radiation and potentially minimize off target toxicity. In addition to synergizing with N, H is an ideal PI3K inhibitor for use in highly angiogenic cancers such as CRC, due to its strong antiproliferative and antiangiogenic properties [18]. Moreover, H is well suited for CRC based on reports of its ability to suppress epithelial-mesenchymal transition and metastasis, and induce necroptosis [28,29].

3.2. Novel HS-173 and niraparib combination induces immunogenic cell death

ICD is a form of regulated cell death that leads to a local antitumor immune response in an otherwise immune-suppressive tumor microenvironment [30,31]. The induction of ICD can trigger an adaptive immune response thereby increasing immune cell infiltration. Select antineoplastic agents, such as oxaliplatin and cyclophosphamide, have been found to trigger ICD [30,32]. The ability of a therapeutic to induce ICD can be assessed through the expression of damage-associated molecular patterns, such as calreticulin (CRT) [33]. Normally constrained to the endoplasmic reticulum, CRT is translocated to the outer leaflet of the cell membrane during ICD [32]. The translocation of CRT acts as an 'eat me' signal, stimulating dendritic cell phagocytosis, which subsequently initiates antigen presentation required for an immune response. Based on this principle, immunogenic chemotherapy has recently been investigated as a route to potentiate checkpoint blockade in multiple tumor models [34–37].

To evaluate the ability of N-H to induce ICD, CT26 cells were treated with the drug combination and stained for membrane CRT expression (Fig. 2A). Colocalization of the cell membrane stain, WGA, with the CRT stain indicated translocation. Here oxaliplatin, which is utilized in the standard-of-care for CRC, was used as a positive control [32,38]. Fluorescence images were taken, and the mean fluorescence intensity of CRT was measured for each treatment. Dose optimization revealed that a concentration as low as 0.8 μM of N-H (0.4 μM each) significantly induces external CRT expression, correlating to ICD (Fig. 2B). N-H demonstrated greater CRT expression than the positive control, oxaliplatin, which required a much higher drug concentration (50 μM) to trigger ICD.

After confirming that N-H induced ICD *in vitro*, we evaluated the ability of this combination to influence immunogenicity in syngeneic CT26 tumors. In this assay, ICD was identified by infiltration of immune cells in necrotic areas, as described by Zhou et al. In this method, strong infiltration was observed 24 h after intratumoral (IT) injection and decreased by day 4 [39,40]. Here, DMSO (control) or N-H was administered IT to separate tumors implanted on the same mouse. After 24 h, tumors were harvested, tissue was fixed, sliced, mounted, and stained for hematoxylin and eosin (H&E). A slice from each tumor was imaged and processed to quantify the percentage of hypoxia, especially in the necrotic core of the tissue, for each treatment (Fig. S2). Based on this evaluation, it appeared that the N-H resulted in slightly increased necrosis as a fraction of total tissue area (6%) compared with DMSO treatment (5%). As visualized in Fig. 2C–F, DMSO and N-H treated tumors displayed not only a difference in tumor composition but also a difference within the necrotic regions. In terms of tumor composition, a clear reduction in tumor cell density, increased immune infiltration, and increased necrosis were observed in the N-H treated tumors. The necrotic regions—identified by an abundant pink staining—allow for identification of ICD-associated alterations. When evaluating the necrotic regions in Fig. 2C & D, the DMSO-treated tumor demonstrates peripheral immune presence (purple leukocyte) and minimal necrotic penetration (dense pink with few purple leukocytes), while the N-H treated tumor (Fig. 2E & F) has increased immune cell infiltration in the necrotic regions. Taken together, this is further evidence that N-H triggers a local immune response by inducing ICD.

3.3. Preparation and characterization of niraparib/HS-173 nanoformulations

After identification of a synergistic treatment regimen that induces ICD, N and H were formulated using a poly(2-oxazaline) (POx)–based amphiphilic triblock copolymer to improve overall drug delivery. Numerous studies have revealed physiological benefits of using POx over the classically used alternative polyethylene glycol (PEG), including higher *in vivo* stability and favorable controlled drug release [20,21,41,42]. Furthermore, POx are less immunogenic than PEG, allowing for repeat dosing [43,44]. Our previous report on the POx polymer A-poly(2-benzyl-2-oxazoline)-A (A-PBzOx-A) suggested it effectively encapsulates highly hydrophobic drugs with aromatic character in small monodisperse micelles with moderate stability [45]. We therefore hypothesized that A-PBzOx-A would effectively encapsulate the hydrophobic and aromatic PARP (N) and PI3K (H) inhibitors as well. Before this report, A-PBzOx-A had not been tested *in vivo,* but *in vitro* no negative effect on the cell viability in primary human dermal fibroblasts was observed, suggesting good cytocompatibility [45]. In addition, similar POx-based ABA triblock copolymers have been shown to be biocompatible [21].

The nanoformulations introduced in this report readily self-assemble via solvent-exchange in an aqueous environment due to the amphiphilic nature of the polymer. A-PBzOx-A is a triblock copolymer with an ABA arrangement where 2 hydrophilic poly(2-methyl-2-oxazoline) ('A') units sandwich a hydrophobic and aromatic poly(2-benzyl-2-oxazoline) ('B') unit. Briefly, N and H were solubilized in DMSO and mixed with A-PBzOx-A in ethanol. This organic phase was then diluted in PBS, at which point drug-encapsulating micelles spontaneously formed, and were subsequently purified from free drug, polymer, and solvent by centrifugal nanofiltration (Fig. 3A). The resulting micelles were found to be stable for a week at room temperature and do not experience changes in size or drug loading after lyophilization and resuspension (Fig. S3). The micelles have an average hydrodynamic diameter of 20.8 nm with a polydispersity index less than 0.2 as determined by DLS (Fig. 3B & S4). Such small size can be considered particularly promising for hard to penetrate tumors with dense stroma [46]. TEM confirmed the presence of spherical micelles with a size of approximately 14 nm (Fig. 3C). Interestingly, the morphology of the particles is altered with drug loading; empty micelles (E POx) have a mix of wormlike and spherical micelles, whereas drug-loaded (N-H POx) boast more spherical but somewhat bigger micelles (Fig. S4). Such morphology changes with drug loading are not uncommon and have been reported previously for similar POx-based micelles [47,48].

As small molecule drug carriers, POx polymers have been cited for highly efficient encapsulation of taxanes and many other compounds of particularly low water solubility [21,49]. Here for the first time, we showed that POx are excellently suited for encapsulating the DDR inhibitor class as well. Evaluation of drug loading by HPLC revealed high encapsulation efficiencies and loading capacities of N and H in the POx micelles (Table S1). These micelles achieved a 5-fold greater molar loading capacity with 8.4 times less polymer (5 mg/mL) than previous poloxamer-DDR inhibitor formulations [15]. Importantly, this enhanced formulation will potentially increase the amount of drug delivered to the tumor and dramatically reduce formulation-associated toxicity. To that end, the plain POx formulation (empty POx; E POx) was evaluated for cytotoxicity and found to be nontoxic across a broad range of concentrations. Furthermore, encapsulation did not appear to affect the toxicity of the N-H combination with or without radiation (Fig. 3D).

Investigating the influence of pH on the release of drug from our formulation revealed differing profiles for the two drugs. N-H drug

release from the dual loaded micelle was evaluated at pH 5.5 (endosomal pH), 6.8 (tumor microenvironment pH), and 7.4 (blood pH). At each pH N reached 80% release within the first 24 h, whereas H only reached ~10% release after 24 h, with maximum release of 33% at pH 7.4 at 2 weeks (Fig. 3E, S5). Although both drugs display similar hydrophobicity, release appears to be highly pH dependent with peak HS-173 release occurring at pH 7.4 and peak N release occurring at pH 5.5. Importantly, while release in a cell-free system is slow and not complete, data presented in Fig. 3D clearly show that drug is reaching the target in the presence of cells, likely via endocytosis. This demonstrates the limited use of drug release studies in a simple dialysis bag setup.

3.4. Clonogenicity and DNA damage

After formulation, the ability of free and encapsulated N-H to induce DNA DSB, which may contribute to tumor immunogenicity, was evaluated. Both N and H act as cell cycle inhibitors, stalling cells in the most radiosensitive phase, G2/M [18,50]. This cell cycle phase is considered more radiosensitive because DNA is condensed, and IR can induce more damage in a single track, reducing the radiation dose needed to cause the same level of DNA damage [51]. Furthermore, H has been shown to inhibit DNA damage repair kinases ataxia-telangiectasia mutated (ATM) and DNA-dependent protein kinase catalytic subunit (DNA-PKcs), which initiate a DSB signaling phosphorylation cascade [52]. Niraparib, on the other hand, prevents the repair of SSBs by inhibiting PARP [50]. Together, H and N prevent effective DNA repair, leading to accumulation of breaks after radiation.

To evaluate DDR inhibition in CRC, the radiation sensitizing potential of N-H was evaluated *in vitro* by monitoring the induction of DSBs and clonogenic survival. Untreated CT26 cells and CT26 treated with carrier (E POx), drug (N-H), or drug formulation (N-H POx) with or without radiation were evaluated by both microscopy and flow cytometry to determine the extent of DSB induction using the surrogate marker, γH2AX [53]. For microscopy, fluorescence images of the treated and stained cells were taken and then the γH2AX were quantified per nuclei (Figs. S6A–B). As observed by both microscopy and flow cytometry, administration of N-H or N-H POx and radiation results in an increase in both number and intensity of DSBs compared with radiation alone or with E POx, demonstrating the radiosensitization potential of N-H (Fig. 4A–C). In addition, by microscopy, the frequency of the γH2AX stain is slightly higher in cells treated with N-H POx compared with N-H, indicating minimally more DNA damage is inflicted when the drugs are formulated (Fig. 4A–B**)**. The slight increase in DNA damage may suggest that the POx formulation is either increasing therapeutic uptake or may be participating in the prevention of DNA damage repair, despite a lack of observed toxicity. Reportedly, numerous amphiphilic POx micelles are quickly endocytosed with distribution throughout the cell, but particularly in the perinuclear region, the proximity of which may explain enhanced DNA damage in the nanoformulation [54]. By *in vitro* analysis, the hydrophilic, uncharged corona of the micelles facilitated comparable CT26 cellular uptake of POx micelles loaded with Cy7.5 dye (Cy7.5 POx) relative to free dye (Fig. S7). The small size of these micelles does not appear to hinder their uptake compared with free drug, supporting the microscopy data showing increased γH2AX with N-H POx. Contrastingly, analysis by flow cytometry showed equivalent γH2AX intensity for N-H and N-H POx (Fig. 4C); however microscopy data are more likely to include dead cells thus making it more reliable when understanding the induction of DNA DSBs.

Then, the clonogenic assay was used to assess reproductive cell death after IR and cytotoxic treatments. Cells are plated at low density, then exposed to drugs and increasing doses of radiation, and monitored for colony formation. In this experiment, cells were incubated with N-H and N-H POx at equal concentrations for 24 h before radiation to assess the impact of micellar delivery. The survival curves in Fig. 4D indicated that N-H POx is more effective than N-H free when exposed to radiation, supporting the above γH2AX microscopy results. Coencapsulation allows a greater chance that both drugs reach the same cell rather than separate cells, which could account for increased synergistic efficacy [41,55-57]. When evaluating the influence of H POx or N POx versus N-H POx, we see that there is a decrease in SF when the drugs are treated together, suggesting sufficient drug release for synergistic radiation sensitization (Fig. S8).

3.5. Efficacy of multimodal combination therapy

Upon validation of *in vitro* efficacy, multimodal (PARP-PI3K, RT, and ICB) therapy was evaluated in tumor-bearing BALB/c mice. Animals were implanted subcutaneously with CT26 cells, and tumors were allowed to develop for seven days until palpable. Seventy-six mice were then randomized into eight treatment groups (four therapy arms delivered with or without radiation) as outlined in the full experimental design (Fig. S9). Four of these groups received intraperitoneal CTLA-4 antibody (α-CTLA-4) injections five days before additional treatment was initiated (Fig. 5A). From each treatment group, four mice were randomized to the treatment efficacy/safety study to be sacrificed on the day the first mouse reached an endpoint. The remaining mice in each treatment group were randomized into the survival study, where sacrifice occurred for each mouse independently when they reached an endpoint. On day 0, micelle (3.57 mg/kg H, 3.69 mg/kg N, 34.1 mg/kg POx) and radiation (1 Gy) treatments commenced and were repeated every other day for a total of three doses each. Tumor growth for all mice was monitored by caliper measurements until the first animal met an endpoint criterion (average tumor diameter greater than 20 mm or ulceration), which occurred on day 14.

N-H POx was administered in three relatively low doses to leverage the drug synergy and ICD observed previously. Here, treatment efficacy is assessed against the carrier (E POx) control for comparison. Utilizing this conservative drug treatment, N-H POx and N-H POx + IR treatment groups did not show significant benefit on the basis of relative tumor volume measurement (Fig. 5B, S10). However, upon evaluation of endpoint (day 14) tumor mass, N-H POx appears to vastly increase the number of mice responding to α-CTLA-4 therapy and to a lesser extent the number of mice responding to IR (Fig. S11). Despite the lack of overall improved tumor growth control of N-H POx alone or added to radiation, histologic evaluation of N-H POx–treated tumors demonstrate tissue-level differences in comparison to the carrier (Fig. 5C and S12-14). To visualize these differences, tumors were harvested at tumor efficacy/safety study end (day 14), formalin-fixed, paraffin-embedded, and stained to visualize hypoxia (H&E), apoptosis (CC3), and proliferation (Ki67). The percentage of stained area relative to the whole tumor slice was quantified, with the N-H POx–treated tumor showing higher percentage of both hypoxic/necrotic tissue and apoptotic tissue compared with E POx (Fig. 5C, S12). Further comparison of these two groups revealed a slight decrease in Ki67 staining, indicating a decrease in tissue proliferation. Previous reports have noted that HS-173 acts as an anti-angiogenic agent which potentially accounts for the increase in hypoxia, as well as a decrease in Ki67 for N-H POx–treated tumors [18,58]. In addition, N-H POx induced beneficial histological changes to α-CTLA-4 treated mice. The addition of N-H POx to the α-CTLA-4 treatments reduced hypoxia and increases apoptosis. N-H Pox + α-CTLA-4 did, however, result in the highest proliferation of the α-CTLA-4 treatments, but the triple combination showed the least Ki67 stain, potentially indicating that the combination of the three treatment modalities is preferential (Figs. S13 and S14). Overall, histological analysis demonstrated tissue-level differences between control and drug-treated tumors which are not evident by evaluation of tumor growth curves. This indicates that administering N-H POx may be a promising strategy to potentiate ICB.

Although tumor size control was not observed with N-H POx treatments under this treatment schedule, the α-CTLA-4 combination treatments proved very effective. Here, we also note that α-CTLA-4 therapy alone was efficacious and demonstrated enhanced tumor control over

radiation alone. Interestingly, previous reports observed that α-CTLA-4 administration (250 μg seven days after tumor implantation) alone did not influence CT26 tumor response or survival [59]. Comparatively, we observed that the E POx + α-CTLA treatment (green curve) exhibited noticeable tumor control in comparison with carrier (E POx) alone. Furthermore, the addition of either N-H POx (brown), IR (purple), or their combination to α-CTLA-4 (navy) all resulted in reduced rate of tumor growth compared with E POx + α-CTLA-4 (green) at day 14 (Fig. 5B).

To further assess tumor control, relative tumor size measurements were continued for the ICB-treated cohort of animals in the survival study (Fig. 5D). This extended time frame allowed for greater separation between tumor growth curves to be observed between the treatment groups. Here, data were only calculated for the entire treatment group until the first animal reached endpoint criteria to maintain statistical values ($n \geq 4$, Fig. S9C). In the absence of IR, after 25 days, mice treated with N-H POx + α-CTLA-4 showed reduced tumor growth rate compared with those treated with the carrier, E POx, + α-CTLA-4. Although tumor growth curves suggest a potential advantage with the multimodal therapy, comparison is limited by the death of an E POx + IR + α-CTLA-4 mouse at day 28.

Ultimately, this initial dosing schedule of N-H POx did not extend survival over E POx for non-ICB treatment groups, with median survival of 14 days for both groups (Fig. S15). While the addition of radiation in these non-ICB groups slightly increased survival, there was no additional benefit when drug was administered (median survival 18 days for both). The addition of ICB demonstrated a significant increase in survival regardless of additional agents used. However, the micelle formulation + α-CTLA-4 (brown) did provide a survival benefit over the POx carrier + α-CTLA-4 (green), increasing median survival from 33.5 to 43 days (Fig. 5E). Furthermore, the additional benefit of including IR in the treatment regimen was clearly demonstrated by both POx (E and N–H) + α-CTLA-4 treatments as median survival increased to 37 and 53 days, respectively.

3.6. Efficacy of a later anti-CTLA-4 dose administration

To elucidate the effect of N-H POx + IR on α-CTLA-4 efficacy, the POx + IR + α-CTLA-4 treatments were repeated with the same ICB dosing schedule as aforementioned (−5 days) and a delayed administration (0 days) coinciding with the start of POx and IR (Fig. 6A & S16). In the aforementioned study, the efficacy of α-CTLA-4 overshadowed sensitization with multimodal therapy. Delaying ICB administration allowed for the development of a more established tumor that may be less likely to be controlled by ICB and RT alone. In mouse models, dosing too early with α-CTLA-4 may deplete regulatory T cells (Tregs) such that the tumor is minimized or cured with combined radiation/α-CTLA-4 before any additional treatment can be administered and evaluated. As mentioned previously, reports have demonstrated the benefits of administering α-CTLA-4 before RT [34]. Tregs dampen the immune response to radiation and may have served to make the previous α-CTLA-4 + radiation treatments (purple and navy curves in Fig. 5B) more efficacious. However, clinically, patients with late-stage CRC are the patient population most often treated with immunotherapy, so the treatment of early-stage tumors with ICB may not accurately reflect clinical routines.

Thus, as the timing of immune checkpoint inhibitor administration may influence therapeutic efficacy, we investigated a later (day 0) ICB administration. Dosing at the later time point resulted in increased tumor control for the uncured, responding mice treated with N-H POx combination versus the E POx, further supporting the use of the multimodal approach (Fig. 6B). At days 31 and 35, the difference in relative tumor volume between the two treatments became significant, before the first mouse reached an endpoint on day 35. In addition, the N-H POx combination with α-CTLA-4 (day 0) was able to delay tumor growth, as evinced in the individual tumor growth curves in Fig. 6C–D with the exception of an individual non-responder in this treatment group. Tumors of mice treated with E POx + α-CTLA-4 (yellow curves) start to rapidly grow at day 25, while that level of growth is delayed to day 45 for N-H POx combination mice (pink curves). As expected, mice treated with α-CTLA-4 on day −5 and either formulation (N-H POx or E POx) saw extremely high cure rates reflecting the need to delay ICB administration to elucidate the effects of incorporating N-H into the therapy regimen (Fig. S17).

While the tumor growth for uncured mice was controlled by the multimodal treatment, the cure rate was not altered with either α-CTLA-4 timing. Early α-CTLA-4 (day −5) resulted in 5 of 7 mice cured in each arm, and late α-CTLA-4 (day 0) led to 4 of 7 in the E POx arm, and 3 of 7 in the N-H POx arm (Table S2A). Ultimately, the cure rate and tumor growth control were high with α-CTLA-4 alone, which suggests lowering the α-CTLA-4 dose would likely emphasize the effect of the N-H POx treatment compared with controls. Finally, the durability of these two combination treatments was analyzed by challenging cured mice with 150,000 CT26 cells on day 58. A small increase in the durability of cure was observed in mice that received N-H POx compared with E POx for early administered α-CTLA-4 (Table S2B).

3.7. Toxicity

Multimodal therapy provides an appealing approach to reduce individual dosing of drug, radiation, and immunotherapy to improve overall safety [60]. To evaluate the safety of this regimen, CT26 tumor-bearing mice receiving the treatment outlined in Fig. 5A, were sacrificed at 14 days to collect blood, organs, and tumors for analysis.

As the DDR inhibitors used in this study can result in myelosuppression leading to dose-limiting toxicities, such as anemia, neutropenia, and thrombocytopenia, and α-CTLA-4 often cause neutropenia as well, we investigated the ability of our nanoformulated combination therapy to reduce such side effects. To assess general overall health, blood chemistry and CBC were run and demonstrated no significant deviation from the E POx control (Fig. 7A–B). Importantly, the only deviation observed was a decrease in aspartate aminotransferases (ASTs) in N-H POx + IR + α-CTLA-4–treated mice (Fig. 7B) and an increase for the non-α-CTLA-4 mice treated with IR and/or N-H POx (Fig. S18A–B). AST, along with alanine transaminase (ALT), is indicative of liver function, and increased expression can indicate liver damage; however the AST levels of all treatments were within a standard range (IDEXX laboratories). This, along with data supporting proper kidney function indicate that this treatment regimen is well-tolerated (see blood urea nitrogen (BUN) in Fig. 7B and S18B).

In addition to blood markers, toxicity was also monitored by evaluating body and organ weight. In Fig. 7C, regardless of treatment group, weight loss indicating gross toxicity was not observed. Furthermore, minimal variation in organ weight is observed between treatment groups (Fig. S19). Interestingly, therapeutic intervention (N-H POx, E POx + IR, and N-H POx + IR) presented a significant reduction in spleen weight as compared with the control, E POx. We attribute the reduced spleen weight in these groups to tumor control, as tumor growth triggers splenomegaly, an accumulation of macrophages and neutrophils [61]. Finally, H&E staining of the harvested organs was performed to further examine the safety of treatment (Fig. 7C & S20). In agreement with the blood and weight data, the H&E images demonstrate no evidence of toxicity and minimal variance between treatment groups with the exception of the livers. Liver histology demonstrated cytoplasmic vacuolization, which can be indicative of tissue damage and possibly a result of exposure to therapeutic agents [62]. Interestingly, treatment with the therapeutic N-H POx decreases liver cytoplasmic vacuolization. Even more surprisingly, vacuolization appears to be further decreased when N-H POx is combined with additional agents, demonstrating the greatest reduction after N-H POx + IR + α-CTLA-4 treatment. Although it is unclear what exactly induces the vacuolization and whether it is harmful, one possible mechanism for this observed decrease in vacuolization is reported to be PARP inhibitor administration [15,63]. Overall,

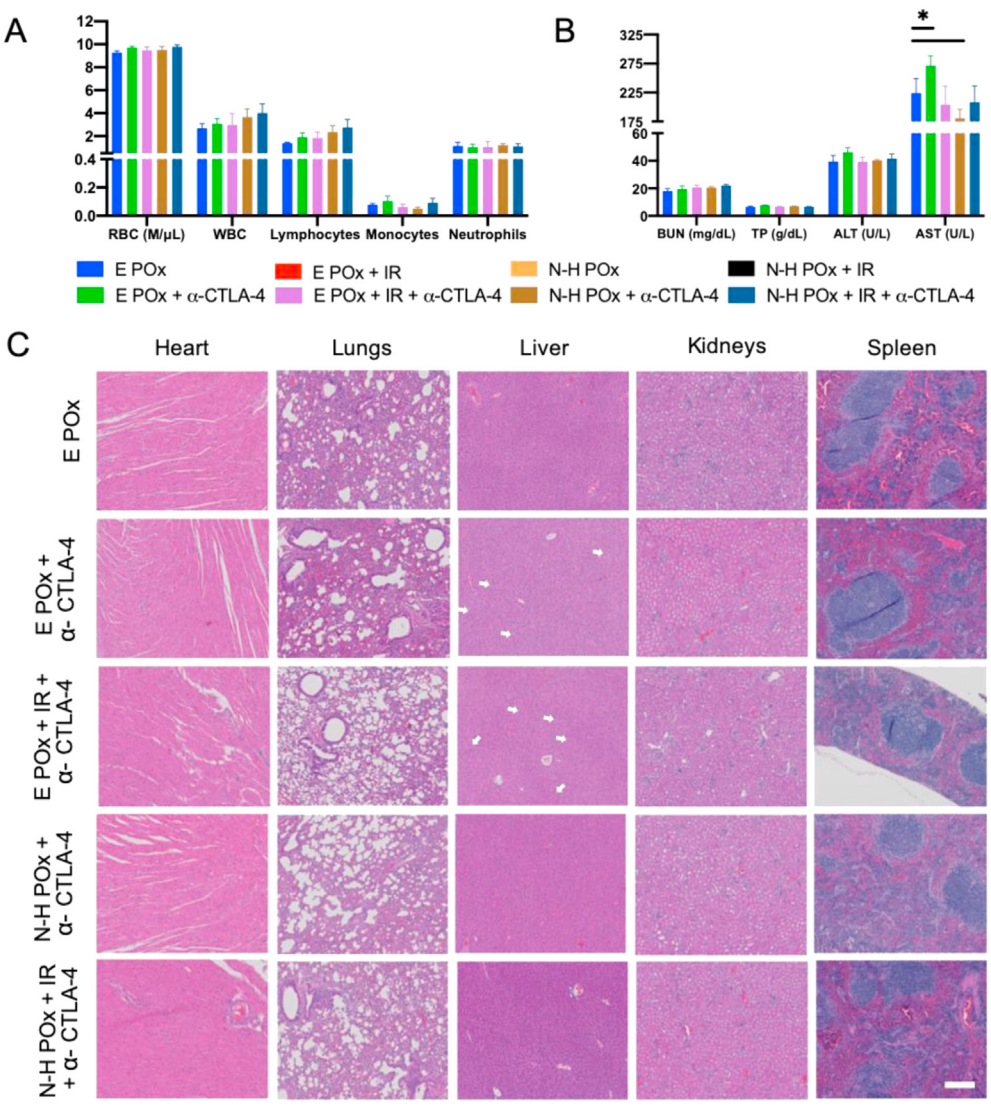

Fig. 7. ***In vivo*** **safety. (A)** CBC results from tumored mice treated after therapeutic regimen in 5A. Counts in K/μL except red blood cells (RBC). **(B)** Clinical chemistry evaluation (BUN, total protein (TP), ALT, AST) demonstrates the absence of organ-based toxicity for all treatment groups. * denotes significance ($p < 0.05$) compared with the E POx control. **(C)** Histologic examination of H&E stained tissues (heart, lungs, liver, kidneys, and spleen) harvested from mice after therapeutic regimen in 5A further confirm the absence of treatment-based toxicity. Scale bar (200 μm) is representative for all images. Arrows indicate areas of hepatic vacuolization. CBC, complete blood count; ALT, alanine transaminase; AST, aspartate aminotransferase; BUN. blood urea nitrogen.

this data provide evidence that the multimodal therapeutic regimen does not result in any appreciable toxicity within the described treatment protocol.

4. Conclusion

Immune checkpoint blockade has been very promising for metastatic CRC. However, clinical application is limited by the toxicity and minimal response in nonimmunogenic tumors. Herein, we proposed a modest drug dosing schedule, with efficacy contingent on a combination of radiation, immunotherapy, and small-molecule inhibitors. By conscientiously combining the inhibitors with radiation and immunotherapy, the doses of all four agents can be lowered, potentially reducing chemoresistance and dose-limiting toxicities. We screened for an optimal radiosensitizing, synergistic PARP/PI3K combination, followed by formulation for increased drug delivery, and validated the combination *in vitro* by assessing the DNA damage, drug release, toxicity, and ability to induce ICD. The novel N-H combination was found to increase DNA damage in CT26 cells and sensitize them to radiation *in vitro*, while simultaneously inducing ICD at a low drug concentration. Upon initial *in vivo* investigation, early dosage of α-CTLA-4 masked the effects of the multimodal therapy, whereas the N-H combination resolutely demonstrated a sensitizing effect in the murine CRC model when α-CTLA-4 was administered at a later time point. Despite a total dose of niraparib 7-fold lower than the clinical daily MTD, niraparib in synergistic combination with HS-173 was able to inhibit tumor growth and trigger ICD. This model indicates first, the promise of the PARP-PI3K combination for CRC, and second, the value of applying immunotherapy agents not only as mono- or dual therapies but as multipronged therapies working in concert.

Data availability

The raw/processed data required to reproduce these findings cannot be shared at this time due to technical or time limitations.

Author contributions

Madeleine R. Landry: Conceptualization, Methodology, Validation, Formal analysis, Investigation, Writing - Original Draft, Writing - Review & Editing, Visualization. **Allison N. DuRoss:** Conceptualization, Methodology, Validation, Formal analysis, Investigation, Writing - Original Draft, Writing - Review & Editing, Visualization. **Megan J. Neufeld:** Methodology, Resources, Writing - Review & Editing. **Lukas Hahn:** Methodology, Resources, Writing - Review & Editing. **Gaurav Sahay:** Methodology, Writing - Review & Editing. **Robert Luxenhofer:** Conceptualization, Writing - Review & Editing, Supervision. **Conroy Sun:** Conceptualization, Methodology, Formal analysis, Resources, Writing - Review & Editing, Supervision, Funding acquisition.

Declaration of competing interest

The authors declare that they have no known competing financial interests or personal relationships that could have appeared to influence the work reported in this paper.

Acknowledgments

M.R.L. and A.N.D. contributed equally to this work.

This work was supported by the NIH NIGMS as a Maximizing Investigators' Research Award, 1R35GM119839-01 (C.S.), NIH NIBIB 1R15EB021581-01 (G.S.) and Oregon State University College of Pharmacy Start-up Funds. R.L. and L.H. gratefully acknowledge support by the Deutsche Forschungsgemeinschaft (DFG, German Research Foundation) project number 326998133 TRR 225 (subproject A03) and project number 398461692, awarded to R.L.

The authors thank the Histology Core, Multiscale Microscopy Core, and Advanced Light Microscopy Core at Oregon Health & Sciences University for their assistance with various procedures presented in this study. The authors also thank Kyle Holmes and Christen Gannett for their contribution to the research. The TOC image was made in ©BioRender -biorender.com.

Appendix A. Supplementary data

Supplementary data to this article can be found online at https://doi.org/10.1016/j.mtbio.2020.100082.

References

[1] Cancer of the Colon and Rectum - Cancer Stat Facts, 2019. Web. 13 Dec. https://seer.cancer.gov/statfacts/html/colorect.html.

[2] J.S. Brown, R. Sundar, J. Lopez, Combining DNA damaging therapeutics with immunotherapy: more haste, less speed, Br. J. Canc. 118 (2018) 312–324, https://doi.org/10.1038/bjc.2017.376.

[3] M.J. Overman, M.S. Ernstoff, M.A. Morse, Where We Stand with Immunotherapy in Colorectal Cancer: Deficient Mismatch Repair, Proficient Mismatch Repair, and Toxicity Management, American Society of Clinical Oncology Educational Book, 2018, pp. 239–247, https://doi.org/10.1200/EDBK_200821.

[4] B. Kc, J.J. Hwang, C.J. Farhangfar, S.J. Chai, Advances in immunotherapy in the treatment of colorectal cancer, Am. J. Hematol/Oncol®. 13 (2017).

[5] A. Kalyan, S. Kircher, H. Shah, M. Mulcahy, A. Benson, Updates on immunotherapy for colorectal cancer, J. Gastrointest. Oncol. 9 (2018) 160–169, https://doi.org/10.21037/jgo.2018.01.17.

[6] M.J. Overman, S. Lonardi, K.Y.M. Wong, H.-J. Lenz, F. Gelsomino, M. Aglietta, M.A. Morse, E. Van Cutsem, R. McDermott, A. Hill, M.B. Sawyer, A. Hendlisz, B. Neyns, M. Svrcek, R.A. Moss, J.-M. Ledeine, Z.A. Cao, S. Kamble, S. Kopetz, T. André, Durable clinical benefit with nivolumab plus ipilimumab in DNA mismatch repair–deficient/microsatellite instability–high metastatic colorectal cancer, J. Clin. Orthod. 36 (2018) 773–779, https://doi.org/10.1200/JCO.2017.76.9901.

[7] A. Bertrand, M. Kostine, T. Barnetche, M.-E. Truchetet, T. Schaeverbeke, Immune related adverse events associated with anti-CTLA-4 antibodies: systematic review and meta-analysis, BMC Med. 13 (2015) 211, https://doi.org/10.1186/s12916-015-0455-8.

[8] T. Sen, B.L. Rodriguez, L. Chen, C.M.D. Corte, N. Morikawa, J. Fujimoto, S. Cristea, T. Nguyen, L. Diao, L. Li, Y. Fan, Y. Yang, J. Wang, B.S. Glisson, I.I. Wistuba, J. Sage, J.V. Heymach, D.L. Gibbons, L.A. Byers, Targeting DNA damage response promotes antitumor immunity through STING-mediated T-cell activation in small cell lung cancer, Canc. Discov. 9 (2019) 646–661, https://doi.org/10.1158/2159-8290.CD-18-1020.

[9] N.M. Reilly, L. Novara, F. Di Nicolantonio, A. Bardelli, Exploiting DNA repair defects in colorectal cancer, Mol Oncol 13 (2019) 681–700, https://doi.org/10.1002/1878-0261.12467.

[10] A. Li, M. Yi, S. Qin, Q. Chu, S. Luo, K. Wu, Prospects for combining immune checkpoint blockade with PARP inhibition, J. Hematol. Oncol. 12 (2019) 98, https://doi.org/10.1186/s13045-019-0784-8.

[11] C. Pantelidou, O. Sonzogni, M. De Oliveria Taveira, A.K. Mehta, A. Kothari, D. Wang, T. Visal, M.K. Li, J. Pinto, J.A. Castrillon, E.M. Cheney, P. Bouwman, J. Jonkers, S. Rottenberg, J.L. Guerriero, G.M. Wulf, G.I. Shapiro, PARP inhibitor efficacy depends on CD8 $^{+}$ T-cell recruitment via intratumoral STING pathway activation in BRCA-deficient models of triple-negative breast cancer, Canc. Discov. 9 (2019) 722–737, https://doi.org/10.1158/2159-8290.CD-18-1218.

[12] P. Cao, Y. Wang, Y. Lv, N. Jiang, L. Zhong, X. Ma, X. Xiao, D. Ding, J. Gu, L. Lin, S. Li, PI3K p110α inhibition sensitizes cervical cancer cells with aberrant PI3K signaling activation to PARP inhibitor BMN673, Oncol. Rep. 42 (5) (2019) 2097–2107, https://doi.org/10.3892/or.2019.7313.

[13] Y.H. Ibrahim, C. García-García, V. Serra, L. He, K. Torres-Lockhart, A. Prat, P. Anton, P. Cozar, M. Guzmán, J. Grueso, O. Rodríguez, M.T. Calvo, C. Aura, O. Díez, I.T. Rubio, J. Pérez, J. Rodón, J. Cortés, L.W. Ellisen, M. Scaltriti, J. Baselga, PI3K inhibition impairs BRCA1/2 expression and sensitizes BRCA-proficient triple-negative breast cancer to PARP inhibition, Canc. Discov. 2 (2012) 1036–1047, https://doi.org/10.1158/2159-8290.CD-11-0348.

[14] A. Juvekar, L.N. Burga, H. Hu, E.P. Lunsford, Y.H. Ibrahim, J. Balmañà, A. Rajendran, A. Papa, K. Spencer, C.A. Lyssiotis, C. Nardella, P.P. Pandolfi, J. Baselga, R. Scully, J.M. Asara, L.C. Cantley, G.M. Wulf, Combining a PI3K inhibitor with a PARP inhibitor provides an effective therapy for BRCA1-related breast cancer, Canc. Discov. 2 (2012) 1048–1063, https://doi.org/10.1158/2159-8290.CD-11-0336.

[15] A.N. DuRoss, M.J. Neufeld, M.R. Landry, J.G. Rosch, C.T. Eaton, G. Sahay, C.R. Thomas, C. Sun, Micellar formulation of talazoparib and buparlisib for enhanced DNA damage in breast cancer chemoradiotherapy, ACS Appl. Mater. Interfaces 11 (2019) 12342–12356, https://doi.org/10.1021/acsami.9b02408.

[16] M.J. Neufeld, A.N. DuRoss, M.R. Landry, H. Winter, A.M. Goforth, C. Sun, Co-delivery of PARP and PI3K inhibitors by nanoscale metal–organic frameworks for enhanced tumor chemoradiation, Nano Res 12 (2019) 3003–3017, https://doi.org/10.1007/s12274-019-2544-z.

[17] N.Y. Jang, D.H. Kim, B.J. Cho, E.J. Choi, J.-S. Lee, H.-G. Wu, E.K. Chie, I.A. Kim, Radiosensitization with combined use of olaparib and PI-103 in triple-negative breast cancer, BMC Canc. 15 (2015) 89, https://doi.org/10.1186/s12885-015-1090-7.

[18] H. Lee, K.H. Jung, Y. Jeong, S. Hong, S.-S. Hong, HS-173, a novel phosphatidylinositol 3-kinase (PI3K) inhibitor, has anti-tumor activity through promoting apoptosis and inhibiting angiogenesis, Canc. Lett. 328 (2013) 152–159, https://doi.org/10.1016/j.canlet.2012.08.020.

[19] K.L. Hennenfent, R. Govindan, Novel formulations of taxanes: a review. Old wine in a new bottle? Ann. Oncol. 17 (2006) 735–749, https://doi.org/10.1093/annonc/mdj100. Ji, J., Zhang, Y., Redon, C.E., Reinhold, W.C., Chen, A.P., Fogli, L.K., Holbeck, S.L., Parchment, R.E., Hollingshead, M., Tomaszewski, J.E., Dudon, Q., Pommier, Y., Doroshow, J.H., Bonner, W.M.: Phosphorylated fraction of H2AX as a measurement for DNA damage in cancer cells and potential applications of a novel assay. PloS One. 12, e0171582 (2017). https://doi.org/10.1371/journal.pone.0171582.

[20] O. Sedlacek, R. Hoogenboom, Drug delivery systems based on poly(2-oxazoline)s and poly(2-oxazine)s, Advanced Therapeutics 3 (2020) 1900168, https://doi.org/10.1002/adtp.201900168.

[21] T. Lorson, M.M. Lübtow, E. Wegener, M.S. Haider, S. Borova, D. Nahm, R. Jordan, M. Sokolski-Papkov, A.V. Kabanov, R. Luxenhofer, Poly(2-oxazoline)s based biomaterials: a comprehensive and critical update, Biomaterials 178 (2018) 204–280, https://doi.org/10.1016/j.biomaterials.2018.05.022.

[22] M.S. Haider, M.M. Lübtow, S. Endres, S. Forster, V.J. Flegler, B. Böttcher, V.O. Aseyev, A.-C. Pöppler, R. Luxenhofer, Think beyond the core: the impact of the hydrophilic corona on the drug solubilization using polymer micelles, ACS Appl. Mater. Interfaces 12 (22) (2020) 24531–24543, https://doi.org/10.1021/acsami.9b22495.

[23] S. Arena, G. Corti, E. Durinikova, M. Montone, N.M. Reilly, M. Russo, A. Lorenzato, P. Arcella, L. Lazzari, G. Rospo, M. Pagani, C. Cancelliere, C. Negrino, C. Isella, A. Bartolini, A. Cassingena, A. Amatu, G. Mauri, A. Sartore-Bianchi, G. Mittica, E. Medico, S. Marsoni, M. Linnebacher, S. Abrignani, S. Siena, F.D. Nicolantonio, A. Bardelli, A subset of colorectal cancers with cross-sensitivity to olaparib and oxaliplatin, Clin. Canc. Res. 26 (6) (2019) 1372–1384, https://doi.org/10.1158/1078-0432.CCR-19-2409.

[24] C. Wang, N. Jette, D. Moussienko, D.G. Bebb, S.P. Lees-Miller, ATM-deficient colorectal cancer cells are sensitive to the PARP inhibitor olaparib, Translational Oncology 10 (2017) 190–196, https://doi.org/10.1016/j.tranon.2017.01.007.

[25] S.A. Danielsen, P.W. Eide, A. Nesbakken, T. Guren, E. Leithe, R.A. Lothe, Portrait of the PI3K/AKT pathway in colorectal cancer, Biochim. Biophys. Acta Rev. Canc 1855 (2015) 104–121, https://doi.org/10.1016/j.bbcan.2014.09.008.

[26] M. Nusrat, J. Roszik, R. Katkhuda, D. Menter, K.P.S. Raghav, V.K. Morris, P. Sharma, J.P. Allison, J.M. Blando, D.M. Maru, M.J. Overman, S. Kopetz, Association of phosphatidylinositol 3-kinase (PI3K) pathway activation with increased immune checkpoint expression in colorectal cancer (CRC) patients, J. Clin. Orthod. 36 (2018), https://doi.org/10.1200/JCO.2018.36.4_suppl.653, 653–653.

[27] T.-C. Chou, Drug combination studies and their synergy quantification using the chou-talalay method, Can. Res. 70 (2010) 440–446, https://doi.org/10.1158/0008-5472.CAN-09-1947.

[28] M. Rumman, K.H. Jung, Z. Fang, H.H. Yan, M.K. Son, S.J. Kim, J. Kim, J.H. Park, J.H. Lim, S. Hong, S.-S. Hong, HS-173, a novel PI3K inhibitor suppresses EMT and metastasis in pancreatic cancer, Oncotarget 7 (2016) 78029–78047, https://doi.org/10.18632/oncotarget.12871.

[29] J.H. Park, K.H. Jung, S.J. Kim, Y.-C. Yoon, H.H. Yan, Z. Fang, J.E. Lee, J.H. Lim, S. Mah, S. Hong, Y.-S. Kim, S.-S. Hong, HS-173 as a novel inducer of RIP3-dependent necroptosis in lung cancer, Canc. Lett. 444 (2019) 94–104, https://doi.org/10.1016/j.canlet.2018.12.006.

[30] L. Bezu, L.C. Gomes-da-Silva, H. Dewitte, K. Breckpot, J. Fucikova, R. Spisek, L. Galluzzi, O. Kepp, G. Kroemer, Combinatorial strategies for the induction of immunogenic cell death, Front. Immunol. 6 (2015), https://doi.org/10.3389/fimmu.2015.00187.

[31] Y.-J. Wang, R. Fletcher, J. Yu, L. Zhang, Immunogenic effects of chemotherapy-induced tumor cell death, Genes Dis 5 (2018) 194–203, https://doi.org/10.1016/j.gendis.2018.05.003.

[32] A. Tesniere, F. Schlemmer, V. Boige, O. Kepp, I. Martins, F. Ghiringhelli, L. Aymeric, M. Michaud, L. Apetoh, L. Barault, J. Mendiboure, J.-P. Pignon, V. Jooste, P. van

Endert, M. Ducreux, L. Zitvogel, F. Piard, G. Kroemer, Immunogenic death of colon cancer cells treated with oxaliplatin, Oncogene 29 (2010) 482–491, https://doi.org/10.1038/onc.2009.356.
[33] M. Obeid, A. Tesniere, F. Ghiringhelli, G.M. Fimia, L. Apetoh, J.-L. Perfettini, M. Castedo, G. Mignot, T. Panaretakis, N. Casares, D. Métivier, N. Larochette, P. van Endert, F. Ciccosanti, M. Piacentini, L. Zitvogel, G. Kroemer, Calreticulin exposure dictates the immunogenicity of cancer cell death, Nat. Med. 13 (2007) 54–61, https://doi.org/10.1038/nm1523.
[34] M. Césaire, J. Thariat, S.M. Candéias, D. Stefan, Y. Saintigny, F. Chevalier, Combining PARP inhibition, radiation, and immunotherapy: a possible strategy to improve the treatment of cancer? Int. J. Mol. Sci. 19 (2018) https://doi.org/10.3390/ijms19123793.
[35] Z. Wang, K. Sun, Y. Xiao, B. Feng, K. Mikule, X. Ma, N. Feng, C.P. Vellano, L. Federico, J.R. Marszalek, G.B. Mills, J. Hanke, S. Ramaswamy, J. Wang, Niraparib activates interferon signaling and potentiates anti-PD-1 antibody efficacy in tumor models, Sci. Rep. 9 (2019) 1853, https://doi.org/10.1038/s41598-019-38534-6.
[36] C. Pfirschke, C. Engblom, S. Rickelt, V. Cortez-Retamozo, C. Garris, F. Pucci, T. Yamazaki, V. Poirier-Colame, A. Newton, Y. Redouane, Y.-J. Lin, G. Wojtkiewicz, Y. Iwamoto, M. Mino-Kenudson, T.G. Huynh, R.O. Hynes, G.J. Freeman, G. Kroemer, L. Zitvogel, R. Weissleder, M.J. Pittet, Immunogenic chemotherapy sensitizes tumors to checkpoint blockade therapy, Immunity 44 (2016) 343–354, https://doi.org/10.1016/j.immuni.2015.11.024.
[37] X. Duan, C. Chan, W. Han, N. Guo, R.R. Weichselbaum, W. Lin, Immunostimulatory nanomedicines synergize with checkpoint blockade immunotherapy to eradicate colorectal tumors, Nat. Commun. 10 (2019) 1899, https://doi.org/10.1038/s41467-019-09221-x.
[38] P. Comella, R. Casaretti, C. Sandomenico, A. Avallone, L. Franco, Role of oxaliplatin in the treatment of colorectal cancer, Therapeut. Clin. Risk Manag. 5 (2009) 229–238, https://doi.org/10.2147/tcrm.s3583.
[39] A. Serrano-del Valle, A. Anel, J. Naval, I. Marzo, Immunogenic cell death and immunotherapy of multiple myeloma, Front. Cell Dev. Biol. 7 (2019), https://doi.org/10.3389/fcell.2019.00050.
[40] H. Zhou, S. Forveille, A. Sauvat, T. Yamazaki, L. Senovilla, Y. Ma, P. Liu, H. Yang, L. Bezu, K. Müller, L. Zitvogel, Ø. Rekdal, O. Kepp, G. Kroemer, The oncolytic peptide LTX-315 triggers immunogenic cell death, Cell Death Dis. 7 (2016), https://doi.org/10.1038/cddis.2016.47 e2134–e2134.
[41] Y. Han, Z. He, A. Schulz, T.K. Bronich, R. Jordan, R. Luxenhofer, A.V. Kabanov, Synergistic combinations of multiple chemotherapeutic agents in high capacity poly(2-oxazoline) micelles, Mol. Pharm. 9 (2012) 2302–2313, https://doi.org/10.1021/mp300159u.
[42] M. Barz, R. Luxenhofer, R. Zentel, M.J. Vicent, Overcoming the PEG-addiction: well-defined alternatives to PEG, from structure–property relationships to better defined therapeutics, Polym. Chem. 2 (2011) 1900–1918, https://doi.org/10.1039/C0PY00406E.
[43] H. Bludau, A.E. Czapar, A.S. Pitek, S. Shukla, R. Jordan, N.F. Steinmetz, POxylation as an alternative stealth coating for biomedical applications, Eur. Polym. J. 88 (2017) 679–688, https://doi.org/10.1016/j.eurpolymj.2016.10.041.
[44] R.W. Moreadith, T.X. Viegas, M.D. Bentley, J.M. Harris, Z. Fang, K. Yoon, B. Dizman, R. Weimer, B.P. Rae, X. Li, C. Rader, D. Standaert, W. Olanow, Clinical development of a poly(2-oxazoline) (POZ) polymer therapeutic for the treatment of Parkinson's disease – proof of concept of POZ as a versatile polymer platform for drug development in multiple therapeutic indications, Eur. Polym. J. 88 (2017) 524–552, https://doi.org/10.1016/j.eurpolymj.2016.09.052.
[45] L. Hahn, M.M. Lübtow, T. Lorson, F. Schmitt, A. Appelt-Menzel, R. Schobert, R. Luxenhofer, Investigating the influence of aromatic moieties on the formulation of hydrophobic natural products and drugs in poly(2-oxazoline)-based amphiphiles, Biomacromolecules 19 (2018) 3119–3128, https://doi.org/10.1021/acs.biomac.8b00708.
[46] H. Cabral, Y. Matsumoto, K. Mizuno, Q. Chen, M. Murakami, M. Kimura, Y. Terada, M.R. Kano, K. Miyazono, M. Uesaka, N. Nishiyama, K. Kataoka, Accumulation of sub-100 nm polymeric micelles in poorly permeable tumours depends on size, Nat. Nanotechnol. 6 (2011) 815–823, https://doi.org/10.1038/nnano.2011.166.
[47] M.M. Lübtow, L.C. Nelke, J. Seifert, J. Kühnemundt, G. Sahay, G. Dandekar, S.L. Nietzer, R. Luxenhofer, Drug induced micellization into ultra-high capacity and stable curcumin nanoformulations: physico-chemical characterization and evaluation in 2D and 3D in vitro models, J. Contr. Release 303 (2019) 162–180, https://doi.org/10.1016/j.jconrel.2019.04.014.
[48] A. Schulz, S. Jaksch, R. Schubel, E. Wegener, Z. Di, Y. Han, A. Meister, J. Kressler, A.V. Kabanov, R. Luxenhofer, C.M. Papadakis, R. Jordan, Drug-induced morphology switch in drug delivery systems based on poly(2-oxazoline)s, ACS Nano 8 (2014) 2686–2696, https://doi.org/10.1021/nn406388t.
[49] M.M. Lübtow, M.S. Haider, M. Kirsch, S. Klisch, R. Luxenhofer, Like dissolves like? A comprehensive evaluation of partial solubility parameters to predict polymer–drug compatibility in ultrahigh drug-loaded polymer micelles, Biomacromolecules 20 (2019) 3041–3056, https://doi.org/10.1021/acs.biomac.9b00618.
[50] D. Caruso, A. Papa, S. Tomao, P. Vici, P.B. Panici, F. Tomao, Niraparib in ovarian cancer: results to date and clinical potential, Ther Adv Med Oncol 9 (2017) 579–588, https://doi.org/10.1177/1758834017718775.
[51] G.I. Terzoudi, G.E. Pantelias, Conversion of DNA damage into chromosome damage in response to cell cycle regulation of chromatin condensation after irradiation, Mutagenesis 12 (1997) 271–276, https://doi.org/10.1093/mutage/12.4.271.
[52] J.H. Park, K.H. Jung, S.J. Kim, Z. Fang, H.H. Yan, M.K. Son, J. Kim, Y.W. Kang, J.E. Lee, B. Han, J.H. Lim, S.-S. Hong, Radiosensitization of the PI3K inhibitor HS-173 through reduction of DNA damage repair in pancreatic cancer, Oncotarget 8 (2017) 112893–112906, https://doi.org/10.18632/oncotarget.22850.
[53] J. Ji, Y. Zhang, C.E. Redon, W.C. Reinhold, A.P. Chen, L.K. Fogli, S.L. Holbeck, R.E. Parchment, M. Hollingshead, J.E. Tomaszewski, Q. Dudon, Y. Pommier, J.H. Doroshow, W.M. Bonner, Phosphorylated fraction of H2AX as a measurement for DNA damage in cancer cells and potential applications of a novel assay, PloS One 12 (2017), e0171582, https://doi.org/10.1371/journal.pone.0171582.
[54] R. Luxenhofer, G. Sahay, A. Schulz, D. Alakhova, T.K. Bronich, R. Jordan, A.V. Kabanov, Structure-property relationship in cytotoxicity and cell uptake of poly(2-oxazoline) amphiphiles, J. Contr. Release 153 (2011) 73–82, https://doi.org/10.1016/j.jconrel.2011.04.010.
[55] X. Wan, Y. Min, H. Bludau, A. Keith, S.S. Sheiko, R. Jordan, A.Z. Wang, M. Sokolsky-Papkov, A.V. Kabanov, Drug combination synergy in worm-like polymeric micelles improves treatment outcome for small cell and non-small cell lung cancer, ACS Nano 12 (2018) 2426–2439, https://doi.org/10.1021/acsnano.7b07878.
[56] X. Wan, J.J. Beaudoin, N. Vinod, Y. Min, N. Makita, H. Bludau, R. Jordan, A. Wang, M. Sokolsky, A.V. Kabanov, Co-delivery of paclitaxel and cisplatin in poly(2-oxazoline) polymeric micelles: implications for drug loading, release, pharmacokinetics and outcome of ovarian and breast cancer treatments, Biomaterials 192 (2019) 1–14, https://doi.org/10.1016/j.biomaterials.2018.10.032.
[57] H.-C. Shin, A.W.G. Alani, H. Cho, Y. Bae, J.M. Kolesar, G.S. Kwon, A 3-in-1 polymeric micelle nanocontainer for poorly water-soluble drugs, Mol. Pharm. 8 (2011) 1257–1265, https://doi.org/10.1021/mp2000549.
[58] S.-M. Yun, K.H. Jung, H. Lee, M.K. Son, J.-H. Seo, H.H. Yan, B.H. Park, S. Hong, S.-S. Hong, Synergistic anticancer activity of HS-173, a novel PI3K inhibitor in combination with Sorafenib against pancreatic cancer cells, Canc. Lett. 331 (2013) 250–261, https://doi.org/10.1016/j.canlet.2013.01.007.
[59] K.H. Young, J.R. Baird, T. Savage, B. Cottam, D. Friedman, S. Bambina, D.J. Messenheimer, B. Fox, P. Newell, K.S. Bahjat, M.J. Gough, M.R. Crittenden, Optimizing timing of immunotherapy improves control of tumors by hypofractionated radiation therapy, PloS One 11 (2016), https://doi.org/10.1371/journal.pone.0157164.
[60] W. Mu, Q. Chu, Y. Liu, N. Zhang, A review on nano-based drug delivery system for cancer chemoimmunotherapy, Nano-Micro Lett. 12 (2020) 142, https://doi.org/10.1007/s40820-020-00482-6.
[61] S. Radoja, T.D. Rao, D. Hillman, A.B. Frey, Mice bearing late-stage tumors have normal functional systemic T cell responses in vitro and in vivo, J. Immunol. 164 (2000) 2619–2628, https://doi.org/10.4049/jimmunol.164.5.2619.
[62] T. Aki, A. Nara, K. Uemura, Cytoplasmic vacuolization during exposure to drugs and other substances, Cell Biol. Toxicol. 28 (2012) 125–131, https://doi.org/10.1007/s10565-012-9212-3.
[63] M. Dönmez, B. Uysal, Y. Poyrazoğlu, Y.E. Öztaş, T. Türker, Ü. Kaldirim, A. Korkmaz, PARP inhibition prevents acetaminophen-induced liver injury and increases survival rate in rats, Turk. J. Med. Sci. 45 (2015) 18–26, https://doi.org/10.3906/sag-1308-48.